

Enabling Renewable Energy Technologies in Harsh Climates with Ultra-Efficient Electro-Thermal Desnowing, Defrosting, and Deicing

Longnan Li, Siavash Khodakarami, Xiao Yan, Kazi Fazle Rabbi, Ahmet Alperen Gunay, Andrew Stillwell, and Nenad Miljkovic*

The rapid anthropomorphic emission of greenhouse gases is contributing to global climate change, resulting in the increased frequency of extreme weather events, including unexpected snow, frost, and ice accretion in warmer regions that typically do not encounter these conditions. Adverse weather events create challenges for energy systems such as wind turbines and photovoltaics. To maintain energy efficiently and operational fidelity, snow, frost, and ice need to be removed efficiently and rapidly. State-of-the-art removal methods are energy-intensive (energy density $> 30 \text{ J cm}^{-2}$) and slow ($> 1 \text{ min}$). Here, pulsed Joule heating is developed on transparent self-cleaning interfaces, demonstrating interfacial desnowing, defrosting, and deicing with energy efficiency (energy density $< 10 \text{ J cm}^{-2}$) and rapidity ($\approx 1 \text{ s}$) beyond what is currently available. The transparency and self-cleaning are tailored to remove both snow and dust while ensuring minimal interference with optical light absorption. It is experimentally demonstrated a multi-functional coating material on a commercial photovoltaic cell, demonstrating efficient energy generation recovery and rapid ice/snow removal with minimal energy consumption. Through the elimination of accretion, this technology can potentially widen the applicability of photovoltaics and wind technologies to globally promising locations, potentially further reducing greenhouse gas emissions and global climate change.

fuel use will lead to higher greenhouse gas emission, which is linked to climate change.^[2] Solar photovoltaic (PV) technologies have attracted a considerable amount of interest as an alternate electricity generation method capable of reducing emissions.^[3] With the technological maturation of PV technology, more than 600 GW of PV capacity has been installed globally.^[4] Photovoltaic power generation is both technologically feasible and economically viable to supply an increasingly larger share of global energy demand. The spatial diversity of promising locations for PVs (high sun irradiance) has led to the suggested installation in regions exposed to snowfall. Snow coverage of PV panels leads to losses in power generation due to blocking of the incoming solar light.^[5] The loss from snow coverage in annual energy production can be as high as 34%, which varies depending on the type of panel and location.^[6] Production loss during the winter can be as high as 100% due to persistent snow coverage.^[7]

1. Introduction

As global population and energy consumption grow, demand of carbon-based fossil fuels will increase.^[1] The increase in fossil

The integration difficulty of renewable energy technologies in attractive locations with harsher climatic conditions has only been exacerbated by the increased occurrence of extreme weather events.^[8] These extreme events can bring


L. Li, S. Khodakarami, X. Yan, K. Fazle Rabbi, A. A. Gunay, N. Miljkovic
Mechanical Science and Engineering
University of Illinois at Urbana-Champaign
Urbana, IL 61801, USA
E-mail: nmiljkov@illinois.edu

L. Li
GPL Photonics Lab
State Key Laboratory of Applied Optics
Changchun Institute of Optics
Fine Mechanics and Physics
Chinese Academy of Sciences
Changchun 130033, China

A. Stillwell, N. Miljkovic
Electrical and Computer Engineering
University of Illinois at Urbana-Champaign
Urbana, IL 61801, USA

N. Miljkovic
Materials Research Laboratory
University of Illinois at Urbana-Champaign
Urbana, IL 61801, USA

N. Miljkovic
International Institute for Carbon Neutral Energy Research
(WPI-I2CNER)
Kyushu University
744 Moto-oka, Nishi-ku, Fukuoka 819-0395, Japan

 The ORCID identification number(s) for the author(s) of this article can be found under <https://doi.org/10.1002/adfm.202201521>.

© 2022 The Authors. Advanced Functional Materials published by Wiley-VCH GmbH. This is an open access article under the terms of the Creative Commons Attribution License, which permits use, distribution and reproduction in any medium, provided the original work is properly cited.

The copyright line for this article was changed on 16 May 2022 after original online publication.

DOI: 10.1002/adfm.202201521

snow and ice to unexpected locations unprepared for cold weather. For example, in February of 2021, a historical cold wave reached the state of Texas in the United States. During the disaster, more than three million people in Texas suffered electricity blackouts. Texas produces the most renewable electricity (without hydropower) in the United States, resulting in capacity loss due in part to shut down from low temperature and heavy snowfall on PV panels and wind turbines.^[9] After snowfall, the ambient temperature can remain depressed (<0 °C) for prolonged periods. Therefore, although sunshine is present, melting of the fallen snow can be delayed and may take several hours to several weeks. To avoid prolonged blackouts, rapid and efficient desnowing methods are needed.

To maintain energy efficiency and operational fidelity of PV and wind energy technologies, snow, frost, and ice need to be removed from the surfaces in a highly efficient and rapid manner. For PV panels, current snow removal methods include manual removal by humans or machines, panel angle adjustment,^[10] passive reflective heating,^[11] anti-icing coatings,^[12] steady electrical heating,^[13] and the application of chemicals.^[14] The majority of existing snow removal methods are based on two physical mechanisms: complete melting of the snow or sliding of the accumulated snow from the panel. Currently, no single snow removal method satisfies the shortcomings of existing methods, including low energy efficiency, slow removal time, and poor operational fidelity. As a result, a reluctance exists to install PV panels in locations with very high snowfall, irrespective of the solar potential (i.e., Northern US and Canada).^[7]

The effect of climate change on wind energy resources is even more sensitive. Increasing carbon dioxide emissions are leading to decreased wind energy potential across the Northern Hemisphere mid-latitudes due to decreased temperature gradients stemming from climate change.^[15] Thus, to enhance wind capacity, it is important to enable the use of wind turbines in harsher and colder climates where icing and frosting are prevalent. Icing and snow accumulation have devastating effects on wind turbine operation. Reliable and Efficient deicing methods can potentially alleviate these effects.^[16] To resolve this problem, many deicing and anti-icing methods have been developed.^[17] Typically, hot air and resistive heaters enable steady deicing of wind turbine blades.^[18] However, the energy consumption and implementation cost of these deicing systems are unsustainable for large-scale integration or application in even harsher climatic conditions.^[16]

In this work, we overcome the snow/frost/ice accretion challenge by developing a multi-functional coating material that synergistically combines two fundamentally differing snow removal mechanisms. By using pulsed Joule heating for interfacial desnowing, defrosting and deicing that synergistically incorporates interfacial Joule heating with controlled surface wettability, we limit the diffusion of heat and experimentally demonstrate three order of magnitude reduction in snow/frost/ice removal time with lower energy demonstrated in state-of-the-art (SOA) steady heating methods. Our method only requires a single pulse of electrical current for heating the surface to completely remove accreted snow, frost, or ice. We limit the diffusion of heat and thermal losses by applying a controlled electrical pulse to the interface. Furthermore, our

multi-functional coating material is self-cleaning to solid particulate matter, enabling higher power output and stability with reduced operational maintenance. We experimentally demonstrate the energy efficiency and accretion removal time of our approach on a real PV cell by integrating our transparent coating on the PV cover glass. Through elimination of accretion, our coating potentially widens the applicability of renewable energy technologies to promising locations previously deemed unfit. Furthermore, our multi-functional coating may be a promising desnowing/defrosting/deicing paradigm shift for other engineering applications.^[19]

2. Results

2.1. Pulsed Joule Heating for Desnowing, Defrosting, and Deicing

The use of Joule heating for removing snow (desnowing), frost (defrosting), and ice (deicing)^[20] from a surface is energetically demanding due to the large latent heat of solid to liquid phase change of ice. Pulsed Joule heating drastically reduces the required energy and time for desnowing, defrosting, and deicing.^[21] **Figure 1a** shows a conceptual schematic to delineate the difference between pulsed Joule heating and steady heating. For steady heating, the majority of input energy is wasted due to the diffusive nature of heat. During steady heating, which has timescales ranging from tens of seconds to several minutes, heat is allowed to diffuse into the snow/frost/ice as well as the substrate, resulting in needless sensible heating. Implementing a pulse of electro-thermal energy fundamentally reduces stray heat diffusion by confining the time allowed for heat transfer. This becomes clear by noting that the thermal diffusion distance ($L_{\text{diffusion}}$) in a solid media with no phase change scales with time (t) as $L_{\text{diffusion}} \sim \sqrt{\alpha t}$, where α , is the thermal diffusivity of the material.^[22] For pulsed Joule heating, the rapid and confined temperature rise near the heater layer results in spontaneous melting of an ultra-thin region (<100 μm) of snow/frost/ice. The formation of the thin lubricating melted layer enables body forces such as gravity to remove the remaining and un-melted snow/frost/ice (**Figure 1b,c**).^[21a,b] When integrated with the glass cover of a snow-covered PV panel (**Figure 1b**, teal color), pulsed Joule heating ensures sliding of the bulk snow layer from the panel (**Figure 1c**) and recovers the electrical energy generation (**Figure 1c**, inset). Thus far, the porous nature of the snow and frost along with their low density compared to ice^[23] have prevented the implementation of pulsed Joule heating for desnowing and defrosting.

2.2. Coating Properties

Combining nanostructures with a conformal hydrophobic coating leads to superhydrophobicity (apparent advancing contact angle $\theta_a^{\text{app}} > 150^\circ$ and contact angle hysteresis $\Delta\theta < 10^\circ$), which enables rapid shedding of liquid by droplet jumping, sliding, and rolling.^[24] To remove partially melted frost or snow from PV panels via pulsed Joule heating, the panel cover glass should be superhydrophobic and transparent to the solar

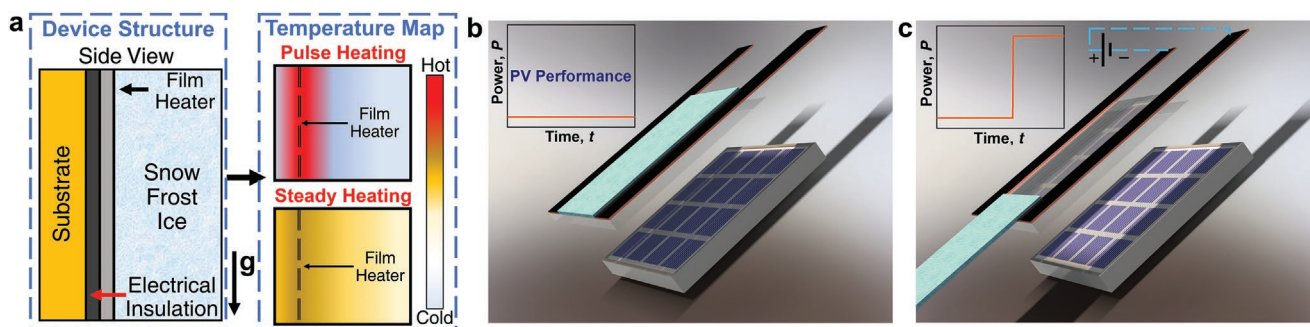


Figure 1. Conceptual schematics of pulsed Joule heating for interfacial heating. a) Conceptual schematic of the working mechanisms of pulsed and steady Joule heating; b,c) Exploded view schematics of the working principle of pulsed interfacial desnowing/defrosting/deicing integrated with a photovoltaics (PV) module where (b) shows the PV module prior to applying the electrical pulse with the surface covered with ice or snow (teal color) and PV current close to zero (inset) and (c) shows the PV module immediately after applying the electrical pulse with the snow/frost/ice sliding from the surface and PV current increasing (inset).

spectrum. To achieve these optical and wetting properties, we developed a simple and ultra-scalable fabrication method for applying superhydrophobic (SHF) coating on a variety of substrates. We first deposited a nanoscale-thick aluminum (Al) layer on the cover glass followed by immersion in hot deionized water to create Al(OH) (boehmite) nanostructures (See Experimental Section and Figure S1, Supporting Information). The wide-band x-ray photoelectron spectroscopy (XPS) spectra of Al 2p and O 1s with selected binding energies reveals the presence of Al and oxygen on both the regular and boehmite samples (Figure S2, Supporting Information). The surface morphology of the as-deposited Al film (50 nm-thick) and boehmite nanostructures coated with a conformal hydrophobic coating (HTMS, see Experimental Section, Supporting Information for details) were characterized with both atomic force microscopy (AFM, Figure 2a) and scanning electron microscopy (SEM, Figure 2b). Statistical analysis of the AFM results indicates that the root mean squared (RMS) roughness of Al film increased from ≈ 2.7 to ≈ 278 nm after the boehmite nanostructure creation (Figure 2a). The grass-like boehmite nanostructures (Figure 2b) maintain a stable Cassie–Baxter state and a very low droplet adhesion that manifests itself in the low value of measured $\Delta\theta$. The Cassie–Baxter state arises when air pockets are trapped inside the structures and therefore the liquid wets a mixture of the solid-gas surface.^[25] This state is in contrast to the Wenzel state where the liquid penetrates to the structures and the apparent droplet contact angle is reduced when compared to Cassie–Baxter state.^[26] The density and porosity of the nanostructures can be modified by varying the immersion time and temperature during fabrication. We chose the conditions used in order to achieve higher superhydrophobicity and minimized droplet–surface adhesion.^[27]

The hydrothermal synthesis of boehmite takes its morphology from dispersed boehmite particles or transformation of the thin film.^[24a,28] The as-deposited Al film on a cover glass substrate became optically transparent after hydrothermal treatment (Figure 2b and inset of Figure 2c). Since the surface roughness is sufficiently small (<30 nm), it does not give rise to visible light scattering.^[29] Moreover, as shown in Figure 2c, the boehmite nanostructures with conformal hydrophobic functionalization achieved apparent advancing contact angles of $\theta_{\text{a}}^{\text{pp}} > 160^\circ$ with an initial as-deposited Al

thickness $h_{\text{Al}} = 10$ nm, which renders the surface superhydrophobic (inset of Figure 2c). Thus, the combination of optical transparency and superhydrophobicity in the same coating allows for multi-functionality to enable pulsed Joule heating for desnowing and defrosting on PV panels. Figure 2e quantifies the effect of the deposited Al film thickness on optical transparency. The boehmite coating shows high transparency not only in the visible spectrum ($\approx 0.3\text{--}0.8\ \mu\text{m}$), but also within the near-infrared spectrum ($<2.0\ \mu\text{m}$). Thicker Al coatings ($h_{\text{Al}} > 100$ nm) resulted in the boehmite coating becoming opaque.

To implement pulsed Joule heating in PV panels, the coating needs to be transparent while achieving the multi-functionality demonstrated thus far. For desnowing of PV panels, the cover glass needs to be capable of efficient pulsed surface heating, superhydrophobicity, and optical transparency. Different materials can be used as Joule heaters, which require capability to concentrate large quantities of heat in a small volume, achieve heating uniformity, good reliability at high temperatures, and corrosion resistance. We used indium tin oxide (ITO) as our heating layer due to its outstanding optical transmittance ($>85\%$) and electrical characteristics.^[30] ITO is electrically conductive ($1\text{--}250\ \Omega\ \text{sq}^{-1}$),^[31] making it suitable for high power density pulsed Joule heating. As an alternative to ITO, a variety of other transparent conductive films (TCF) have been developed. TCFs come in forms such as aluminum-doped zinc oxide (AZO) and gallium-doped zinc oxide (GZO).^[32] Metal nanowires and metal meshes such as silver nanowires (AGNW) or silver/gold meshes have been also used.^[32,33] Carbon nanotubes (CNTs), graphene, and Poly(3,4-ethylenedioxythiophene) (PEDOT) are other examples of TCFs.^[34] Among these options, CNT films have the highest potential as an alternative for ITO due to their similar electrical conductivity ($\approx 10^4\ \text{S cm}^{-1}$) and optical transparency.^[35]

To optimize the multifunctionality of our coating, we investigated different design combination for the superhydrophobic coating and ITO glass to find the best material candidate for PV applications. A variety of ITO glass samples with low sheet resistance ($R_s = 4\text{--}10\ \Omega\ \text{sq}^{-1}$, ≈ 200 nm ITO thickness) and high sheet resistance ($R_s = 70\text{--}100\ \Omega\ \text{sq}^{-1}$, ≈ 30 nm ITO thickness) were selected to combine with the SHF boehmite coating both on the same side of a glass (boehmite layer on top of ITO layer), as well as the back side

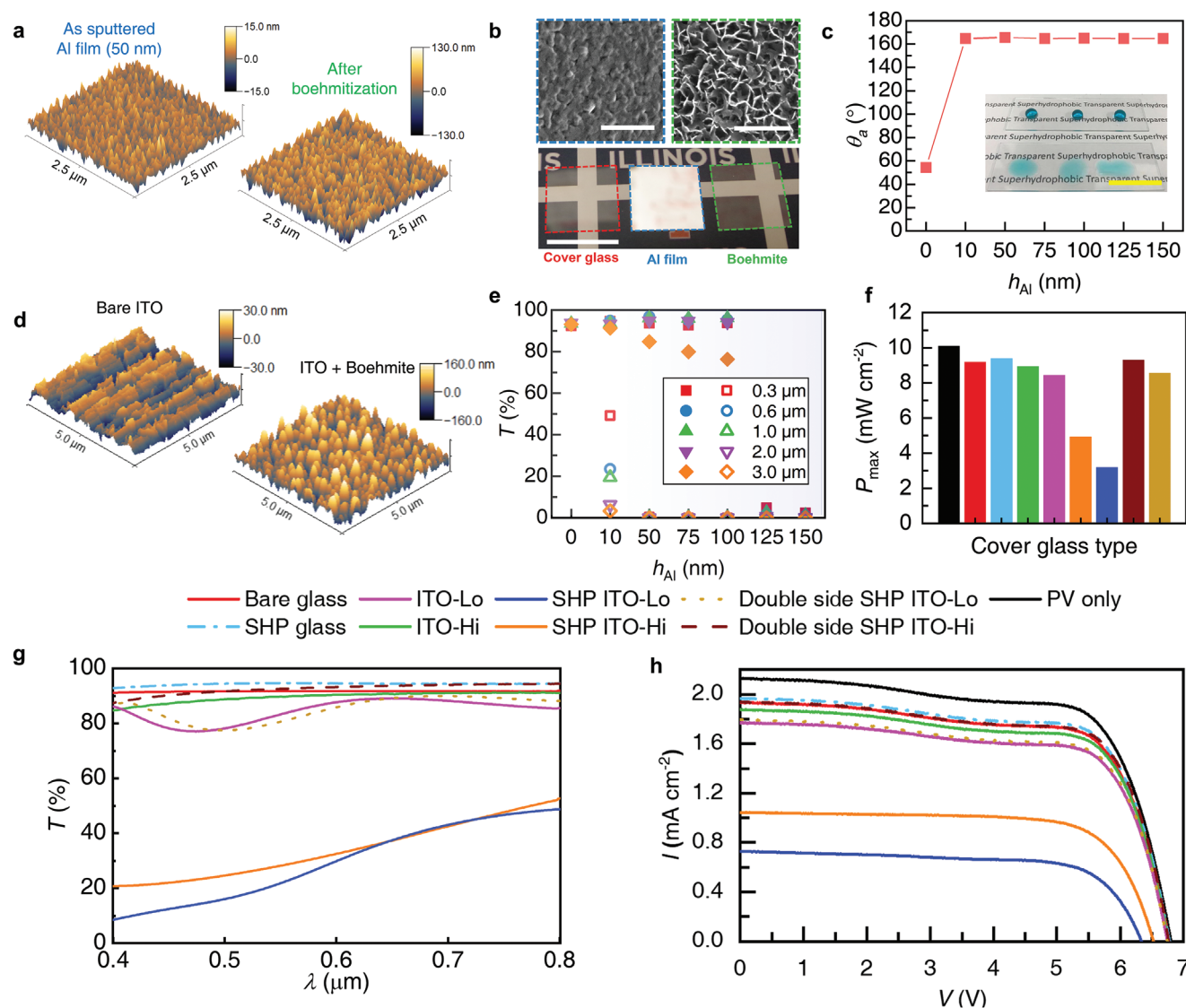


Figure 2. Structure, surface wettability, and optical properties of boehmite coating. a) AFM scanning of as sputtered aluminum film ($h_{Al} = 50$ nm, left) and after boehmite formation (right). b) SEM images for as-deposited aluminum film (upper left) and boehmite nanostructure (upper right). Scale bars are both 500 nm. The bottom image shows the appearance of samples for bare cover glass, with aluminum film and boehmite, respectively. Scale bar: 2 cm. c) Apparent advancing contact angle of water (θ_a^{app}) with different h_{Al} . The inset picture shows water droplet on boehmite coated glass surface (upper) and bare glass surface (bottom). Scale bar: 2 cm. d) AFM of a bare ITO surface and a boehmite coating on the ITO surface. e) Transmittance of as sputtered aluminum sample (blank symbol) and a boehmite coated sample having different h_{Al} . The symbol shape indicates the selected wavelength from full measurement (see full scan data in Figure S5, Supporting Information). f) Maximum power density (P_{max}) of a PV cell integrated with different cover glasses. g) Measured transmittance of all coated cover glasses as a function of wavelength (λ). h) Measured PV cell current-voltage characteristics. The legends for (f), (g), and (h) are the same.

of the glass. The boehmite coating thickness used was fixed as $h_{Al} = 50$ nm.

Samples with single layer coatings (ITO-Hi: high sheet resistance ITO layer on glass, ITO-Lo: low sheet resistance ITO layer on glass and SHP-Glass: boehmite nanostructured SHP glass) maintain as high of a transmittance as measured on bare glass samples (See Figure S3, Supporting Information). For samples with two coating layers (ITO and boehmite), the transmittance changed. Samples with two coatings on the same side (SHP-ITO-Hi: SHP boehmite coating on high resistance ITO layer; and SHP-ITO-Lo: SHP boehmite coating on

low resistance ITO layer) showed semi-transparency. However, when the two coatings were separated on each side of the glass substrate (double side samples), they showed transparency as good as the bare glass sample. The semi-transparency of the single-sided coating is attributed to increased light scattering due to the increased roughness from the ITO and boehmite layers.^[36] The roughness for transparent film formation needs to be <100 nm to ensure good transparency,^[29] which is comparable with the double layer roughness length scale shown in Figure 2d. Figure 2g shows the measured transmittance of each surface (See Experimental Section,

Supporting Information). Analogous to the photographs in Figure S3 (Supporting Information), SHP-ITO-Hi and SHP-ITO-Lo showed lower transmittance in the entire tested wavelength spectrum. Due to the anti-reflective properties of the boehmite SHP layer, double-sided coating of samples with high sheet resistance (Double side SHP ITO-Hi) ensured the same transmittance levels when compared to bare glass. For applications where optical transparency is important, our results indicate that applying the coatings on opposite sides results in transparency as high as bare glass. For PV applications where optical transparency is essential, the ITO layer and the superhydrophobic layer should be coated on opposing sides. Doing so will increase heat losses caused by the intermediate glass layer. However, the energy losses when the heating layer is on backside can be minimized by minimizing the thickness of the glass such that it will minimally affect the efficiency of pulsed Joule heating.

The boehmite coating not only shows minimal impact on optical properties of the substrate, in fact, it increases transmittance of the glass sample when compared to bare glass. We quantified the reflectance of bare and boehmite coated ($h_{Al} = 50$ nm) glass samples as a function of polarized incident angle and wavelength. The boehmite coating reduces the reflectance when compared to the uncoated glass, especially at shorter wavelengths and smaller incident angles (See Figure S4, Supporting Information). When compared to commercial anti-reflective coatings (ARCs), our coating shows comparable performance to nanostructured ARCs^[37] at wavelengths ranging from 300 to 800 nm. The boehmite intersected platelet structure mimics the sharp edges used in developed ARCs.^[37]

To demonstrate the energy impact of the fabricated cover glasses, a commercially available PV cell was tested in a solar simulator (See Section S11 of the Supporting Information). Each of the cover glasses was integrated on top of the PV cell and the cell performance was measured under a fixed light intensity (1 sun ≈ 99 mW cm⁻²). Figure 2f,h shows the current–voltage (I – V) characteristics and maximum power density (P_{max}), of the PV cell integrated with each cover glass. In agreement with the optical transmittance trends (Figure 2g; Figure S3, Supporting Information), double-sided SHP ITO coatings with low sheet resistance (9.29 mW cm⁻²) showed higher P_{max} when compared to bare cover glass (9.18 mW cm⁻²). The semi-transparent nature of the single-sided coating is attributed to increased light scattering due to the increased roughness from the combination of ITO and boehmite layers (hierarchical structures), which results in reduced power output. This indicates that in addition to enabling pulsed desnowing, defrosting, deicing, and self-cleaning, the double side coating method provides additional benefit to the optical properties of PV cells.

2.3. Experimental Characterization of Pulsed Interfacial Desnowing and Defrosting

To achieve ultra-efficient and ultra-rapid snow/frost/ice removal, we developed a multi-functional surface that combines superhydrophobicity, optical transparency, self-cleaning, and enables electro-thermal pulsed Joule heating near the

snow/frost/ice-substrate interface. Removal of snow and frost using pulsed Joule heating has not been achieved in the past due to wicking of the thin melted layer into the porous snow and frost. To characterize the ability of our interfaces to remove naturally grown frost from ambient humidity, high power density pulses were applied to the ITO layer surface while measuring the required power density and energy density to achieve frost removal. Irrespective of surface energy, lower defrosting energy is required when smaller pulse widths are used. Fundamentally, this occurs because at higher heating times, more heat is allowed to diffuse to the bulk substrate. Figure 3a shows finite volume method simulation results (See Section S3 of the Supporting Information) of defrosting of a glass substrate coated with a 1 μ m-thick ITO layer with convection heat transfer on one side (air side) and a constant temperature on the other side (cold plate side). The top and bottom boundaries were adiabatic due to symmetry. Shorter pulse widths ensure more frost melting, with higher spatial confinement of heat near the ITO region. Conversely, with the same input energy, the melt fraction decreases with increased pulse width as the spatial confinement of heat degrades.

To verify the simulation results, experiments were conducted on an experimental setup (see Figure S6, Supporting Information). The surface temperature was kept at -10 °C \pm 2 °C and the relative humidity was 50% \pm 5% for all experiments. Typically, the required defrosting energy decreases with decreasing pulse width (pulse Joule heating time). The experiments demonstrate defrosting energy densities <10 J cm⁻² (Figure 3b,c; Figure S8, Supporting Information). When defrosting on ITO surface, all frost melted with droplets remaining adhered to the surface due to the surface intrinsic hydrophilicity and the ability of the frost to wick the melt. To overcome this challenge and to enable only melting of a several micron thick interfacial lubricating layer to allow frost sliding (Video S1, Supporting Information), we took advantage of superhydrophobic boehmite nanostructures (Figure 2a–c) via direct integration on top of the ITO (SHP ITO). To achieve removal of porous frost and snow, surfaces having high apparent advancing water contact angles (θ_a^{app}) and low contact angle hysteresis ($\theta_a^{app} - \theta_r^{app} = \Delta\theta$, where θ_r^{app} is the apparent receding contact angle) are required. Applying a power density of 0.83 W cm⁻² to frost grown on the SHP ITO resulted in full melting with a required energy density of 23.7 J cm⁻² ($\Delta t_{pulse} \approx 28.5$ s, Video S2, Supporting Information). As a comparison, a one-second electrical pulse with power density of 9.2 W cm⁻² was applied to the same surface to achieve pulsed Joule heating for defrosting (Video S1, Supporting Information). The pulsed method had a 61% decrease in energy consumption when compared to the heating for 28.5 s at 0.83 W cm⁻². The energy reduction translates to a 145 kJ m⁻² reduction in defrost energy consumption per defrosting cycle of a 1 m² polycrystalline Si PV panel. Previous studies have reported desnowing energies on solar cells ranging from 150 to 1200 kJ m⁻², depending on inclination angle and the amount of snowfall.^[13] These values indicate that the reduction in desnowing energy density using our pulsed method is significant for many conditions.

A second advantage of pulsed defrosting on SHP ITO is that the defrosting energy does not increase with frost thickness. To achieve pulsed defrosting, melting of an ultra-thin (<100 μ m)

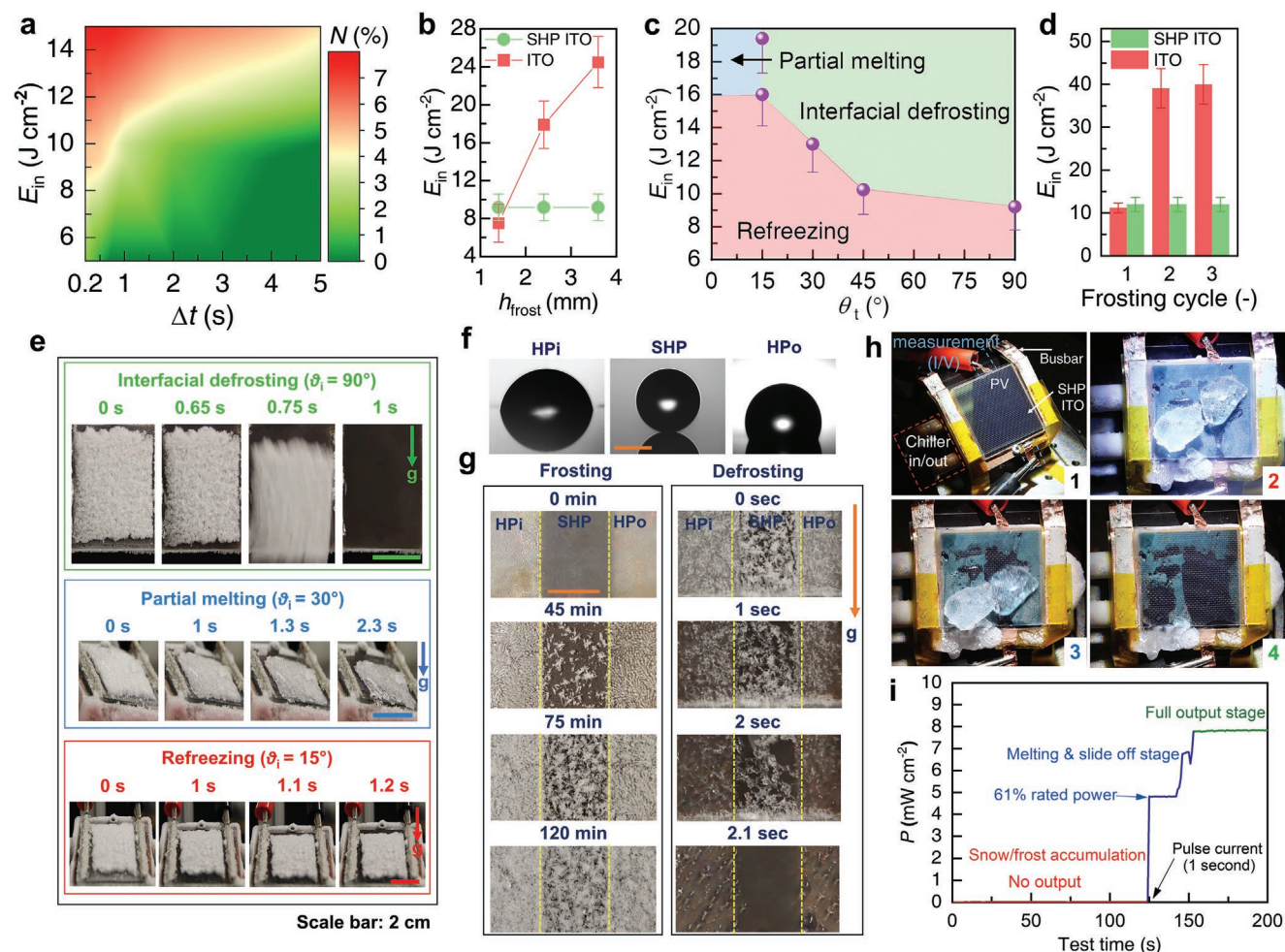


Figure 3. Pulsed interfacial desnowing and defrosting performance. a) Simulation results showing melt fraction as a function of pulse time and input energy on an ITO substrate (See Experimental Section, Supporting Information). b) Required defrost energy density on ITO and SHP ITO as a function of frost thicknesses (freezing time). c) Defrosting regime map. Data points not on boundaries are omitted for clarity. d) Required defrosting energy density for three consecutive frosting/defrosting cycles without cleaning the surface after each cycle. e) Photographs of three different defrosting regimes observed with pulsed Joule heating on SHP ITO on substrates with tilt angle $\phi = 90^\circ$, 30° , and 15° . f) Water droplet images on hydrophilic (HPI) ITO (left), SHP ITO (middle) and hydrophobic (HPO) ITO (right). g) Time-lapse images of two-second pulse defrosting on HPI ITO, SHP ITO, and HPO ITO having a two-hour frost layer. h) Photographs showing the demonstration of pulse desnowing and defrosting on a PV cell with double-sided SHP-I TO-Hi cover glass. Image labels: 1) Initial conditions. 2) With frost and ice. 3) Right after 1 s pulse. 4) Steady condition after pulse. 3 and 4 have the same scale as 2. The SHP ITO sample size is 5×7.5 cm. i) Power density variation of the tested PV cell during the pulse defrosting demonstration with the multi-functional double-sided SHP-I TO-Hi cover glass. Scale bars: (e) 2 cm, (f) 100 μm , and (g) 1 cm.

layer is enough for the remaining frost to slide from the surface. In fact, increasing the thickness of the accumulated frost or snow aids in removal due to the higher mass and resulting gravitational force. Figure 3b plots the experimentally measured energy required to remove different thicknesses of frost. The defrosting energy on SHP ITO is constant. In contrast, melting of the entire frost layer on ITO (melting regime) depends on frost thickness, requiring more energy for longer frosting times (higher thickness). Compared with the one-hour frosting result, the required defrosting energy increased by 138% and 226% for 2 and 4 h frosting times, respectively, while operating in the melting regime (ITO).

In addition to our demonstrated defrosting on vertical surfaces, defrosting on tilted surfaces is important for renewable energy technologies such as PV panels and turbine blades.

On a tilted surface, more time is required for the bulk snow/frost/ice to slide from the surface after melting the thin lubricating layer. Therefore, a larger thickness of snow/frost/ice needs to be melted to ensure that the remaining sliding layer has enough time to slide from the surface before refreezing occurs.^[38] The critical thickness of the melted water layer can be calculated through a force balance between the gravitational force and the transient and velocity-mediated shear force. Assuming a Couette flow for the thin lubricating melted water layer, the critical thickness scales as, $t_c \sim \mu_w \nu / h \rho g \sin \phi$, where μ_w is the melt water dynamic viscosity, ν is the sliding speed, h is the snow/frost thickness, ρ is the ice/frost/snow density, g is the gravitational constant, and ϕ is the tilt angle ($\phi = 90^\circ$ for a vertical surface). Accordingly, t_c increases on a tilted surface and therefore more energy is required to melt a thicker

lubricating water layer (Figure S7, Supporting Information). Using the same defrosting power for the vertical surface may result in refreezing on the tilted surface.

To characterize the effect of tilt, we implemented pulse defrosting for surfaces oriented at $\phi = 45^\circ$, 30° , and 15° (Figure 3e; also see Videos S3 and S4, Supporting Information). Although the minimum required defrosting energy increased with decreasing θ_l (Figure 3c), it was still more efficient when compared to conventional steady heating methods. For a one-second pulse, three different regimes of interfacial defrosting, melting, and refreezing were observed. On highly tilted surfaces ($\theta_l = 15^\circ$), lower power densities ($<16 \text{ W cm}^{-2}$) applied for a one-second pulse could not ensure complete frost removal from the surface. However, higher power densities ($>19 \text{ W cm}^{-2}$) resulted in partial melting of the frost. Therefore, a 3 mm-thick frost layer was not thick enough to achieve interfacial defrosting on highly titled surfaces ($\theta_l < 15^\circ$). The results presented in Figure 3c,e are for a constant sample size (area: $5 \times 5 \text{ cm}$). Increasing the sample size increases the length that snow/frost/ice needs to slide to be fully removed from the surface. Consequently, more time is required for complete frost removal on larger surfaces. A force balance between the shear forces and gravitational forces applied to the snow/frost/ice layer demonstrates how the frost vertical position (x) varies with time and t_c , $x \sim (g \sin \phi t_c \rho (h - t_c) / \mu_w) (t + t_c / \mu_w \rho (h - t_c) (\exp(-t \mu_w / t_c \rho (h - t_c)) - 1))$ (see Note S1 in Supporting Information for details). A second concern with larger area surfaces is Joule heating uniformity at short pulse times. The heating uniformity mainly depends on the quality of the thin-film heater. We tested pulsed Joule heating on a larger 100 cm^2 sample and demonstrated efficient frost removal on the larger surface (See Video S11, Supporting Information). In addition to energy efficiency enhancement, pulsed Joule heating for desnowing and defrosting enable time savings. The time to defrost is key to the overall efficiency as it dictates downtime and lost energy generation. Our method is ultra-rapid ($\approx 1 \text{ s}$), eliminating downtime.

The definition of self-cleaning involves the capability of the surface to remove solid or liquid particulate matter.^[39] Ensuring successful liquid droplet removal from the surface is a significant consideration for energy technologies via the delay of frost nucleation on a superhydrophobic surface.^[40] Refrosting or re-freezing is a significant concern if the surface cannot self-clean itself to a pristine state (no liquid remaining). Re-freezing of remaining liquid droplets occurs much faster when compared to the initial frosting/freezing process due to remnant liquid droplets acting as sources for ice nucleation with reduced thermodynamic energy barrier.^[38] To delay frost buildup, it is critical to ensure rapid removal of condensate droplets from the surface after defrosting or during condensation frosting. If droplets are not removed, refreezing can occur. On hydrophilic ITO, refreezing increases the defrost energy by 250% (Video S5, Supporting Information). The measured defrosting energies for three consecutive frosting/defrosting cycles are shown in Figure 3d. Although a dramatic increase in required defrost energy was observed from first to second cycle, the required energy remained constant for the following cycles due to the approximately constant number of droplets on the surface after each defrosting period (Video S5, Supporting Information). The hydrophobic ITO surface (Figure 3f,g) was

not able to achieve droplet shedding, indicating the importance of minimizing contact angle hysteresis ($\Delta\theta$) to achieve successful droplet removal. The hysteresis of the hydrophobic ITO was $\Delta\theta = 45^\circ$ (Figure S9, Supporting Information), resulting in high adhesion between the droplet and the surface and pinning after defrosting (see Note S2 in Supporting Information for details).

To further investigate the limit of maximum allowable $\Delta\theta$ while ensuring successful pulsed desnowing and defrosting, we fabricated an ITO surface with θ_a^{app} as high as 160° while keeping $\Delta\theta > 10^\circ$ ($\Delta\theta = 13^\circ$) by depositing a $\approx 5 \text{ nm}$ -thick Al film on top of the ITO and forming nanostructures (See Experimental Section, Supporting Information). Despite the high θ_a^{app} , complete droplet removal was not achieved due to the significant $\Delta\theta$. The results emphasized the need for having ultra-low $\Delta\theta$ (SHP ITO, $\Delta\theta = 1^\circ$) to achieve effective pulsed Joule heating for defrosting.^[41] High θ_a^{app} ($>150^\circ$) with the coexistence of hydrophobic nanostructures does not guarantee low $\Delta\theta$ ($<10^\circ$). When structures are nanometric in length scale, it is possible to achieve high liquid–solid contact area, resulting in increased droplet adhesion.^[42] In this case, water can penetrate into the nanostructures and molecular forces such as van der Waals interactions increase droplet–surface adhesion.^[43] If the nanostructures can entrap more air underneath the liquid, this will further decrease the surface energy of the composite interface and cause a reduction in droplet–surface adhesion and $\Delta\theta$.^[38]

To verify the PV desnowing performance of the double-sided SHP-ITO-Hi cover glass, a frost layer was grown with subsequent addition of ice and its slush to emulate accretion. Figure 3h,i show time-lapse photography demonstrating snow/ice removal from the PV cell with pulsed Joule heating as well as the measured power output, respectively. At the initial condition (Figure 3h-1), the PV cell was simply integrated with the double-sided SHP-ITO-Hi cover glass having the ITO heating layer facing downward. When the frost and ice covered the PV cell, the power output was nearly zero due to light blocking (Figure 3h-2 and red line in Figure 3i). After we applied the pulse current to the ITO layer for 1 s, the interfacial layer of frost and ice was rapidly melted and frost and ice started to slide off from the PV cell. The power density of the PV cell recovered to $\approx 61\%$ of its steady clean condition right after the pulse and increased continuously along with the sliding motion of frost (Figure 3h-3 and blue line in Figure 3i). After the majority of frost and ice was removed from the surface, the power output recovered (Figure 3h-4 and green line in Figure 3i).

2.4. Self-Cleaning

The water repellency of the superhydrophobic boehmite not only works in synergy with pulsed desnowing and defrosting to remove accreted material and melted droplets to prevent re-freezing, but also enables self-cleaning during rain and water condensation (dew formation) on PV panels.^[44] Self-cleaning implies that the cleaning function does not require any external stimulus. Thus, a surface can remain clean by repelling contaminants independent of the time of day and weather conditions. Self-cleaning on a superhydrophobic surface can happen

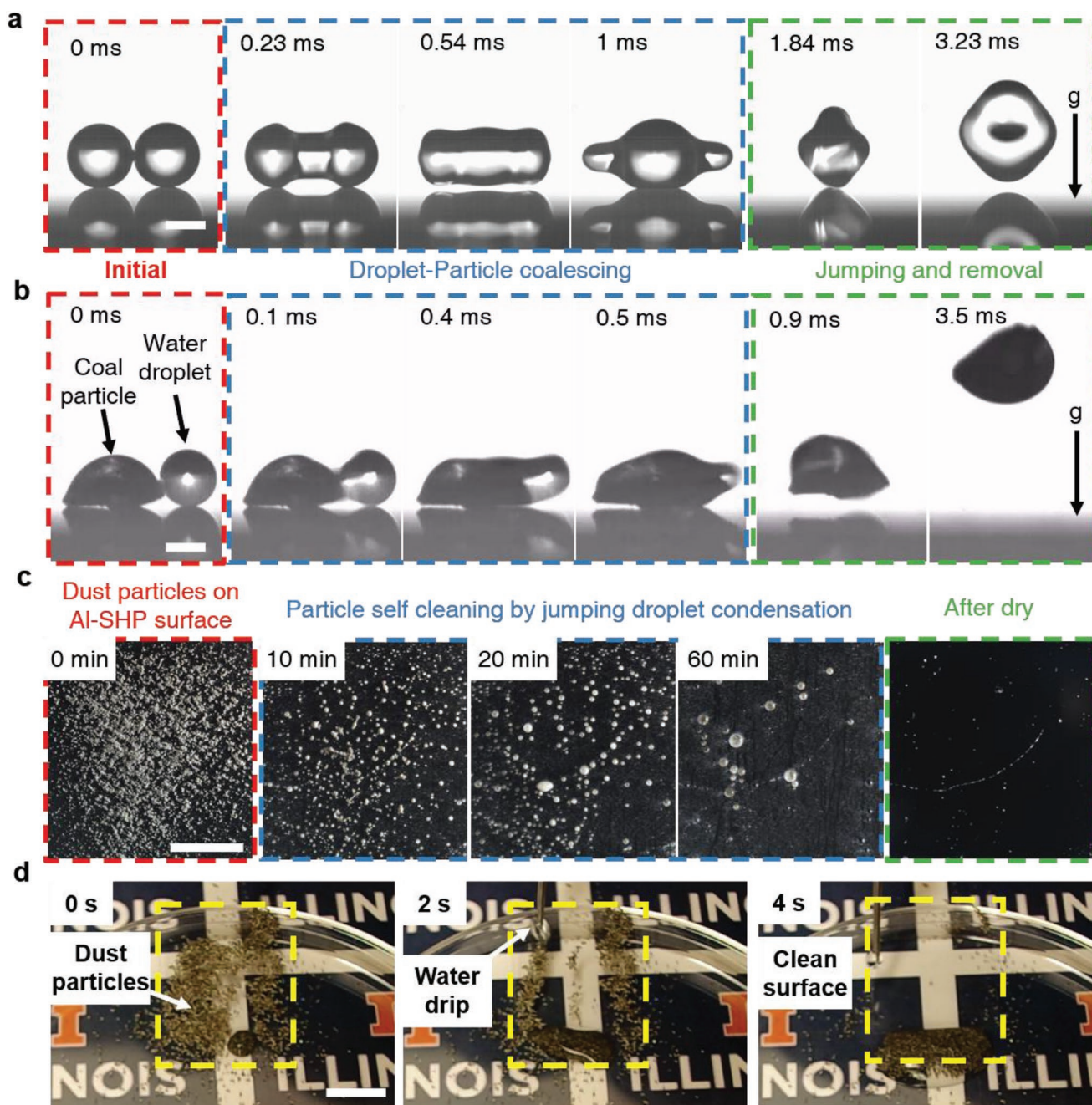


Figure 4. Microscale and macroscale self-cleaning on SHP ITO. Time-lapse high-speed images of coalescence-induced jumping of a) two microscale water droplets, and b) a single microscale water droplet and a dust particle on SHP ITO. c) Time-lapse images of dust particle self-cleaning on SHP ITO via condensation and dew formation. d) Time-lapse images of cleaning with deposited macroscale water droplets to emulate rain. Scale bars: (a) 300 μm , (b) 100 μm , (c) 1 cm, and (d) 1 cm.

due to coalescence-induced droplet jumping.^[45] However, not all superhydrophobic coatings enable droplet jumping, hence not all superhydrophobic surfaces guarantee self-cleaning function.^[27,46] Self-cleaning is achieved on our SHP ITO surface in two ways: dust particle or particulate removal by self-jumping of micro sized water droplets during condensation of dews (water condensation, **Figure 4a–c**), or macroscale water droplet impact (rain droplets, **Figure 4d**) that can collect dust and particulate matter as they shed from the superhydrophobic surface.

Figure 4a shows microscopic visualization of droplet–droplet interactions on our SHP ITO surface. Two microscale droplets coalesce and the formed droplet jumps from the surface in the perpendicular direction and independent of gravity due to surface-to-kinetic energy transfer.^[47] By replacing one of the droplets with a microscale dust particle, we observed that coalescence and jumping is maintained, representing key mechanisms of microscale self-cleaning functionality.^[48] To quantify the efficacy of microscale self-cleaning at the macroscale, artificial dust

particles were intentionally spread on an SHP ITO surface followed by condensation to emulate atmospheric dew formation (See Experimental Section, Supporting Information). As shown in Figure 4c, dust particles were cleaned completely within 1 h. Cleaning by macroscale water droplets to emulate rainfall was successfully demonstrated by applying a water drip towards the SHP ITO surface covered with dust particles (Figure 4d).

Although permanent pollution/soiling (i.e., cemented particles) can occur, we did not consider this condition here. The majority of pollution/soiling mechanisms on PV panels are characterized by the accumulation of removable dust and soil on top of the coating surface, which can be removed by water easily (rain, snow, or washing of the panels) as shown in Figure 4.

2.5. Energy Savings and Applicability

Figure 5a compares our pulsed defrosting method on SHP ITO with other SOA technologies. Our pulsed method requires less energy and is much faster when compared to conventional methods. Although the intermediate heating methods summarized in Figure 5a are comparable to our technology, they have disadvantages. These include either limitation for deicing use only (SOA pulse methods) or an order of magnitude longer heating time (Joule heating methods). Our multifunctional coating design enables rapid (<1 s) accretion removal as well as broad applicability for ice, frost, and snow mitigation by synergistically using pulsed Joule heating and surface engineering.

For a better assessment of the energy impact of pulsed Joule heating for desnowing on a PV system, we calculated and compared the energy consumption of our pulsed Joule heating method, the total power generation by PV cell, and the lost energy of PV cell due to snow coverage. All calculations were conducted using the AM1.5 standard condition. We extracted real temperature and snow depth data for the months of January, February, November, and December of 2020 at two different locations (Chicago, IL, USA and Fairbanks, Alaska, USA).^[49] Single crystal silicon PV cells and five-junction GaAs PV cells were used to investigate the effect of PV cell efficiency on total energy impact (see Note S4 in Supporting Information for calculation methodology). Figure 5b shows the ratio of the energy input for snow removal to the PV cell power generation while using the pulse method and the natural melting method. The proportion of energy consumed by pulse desnowing is <1% of the total generated power for both PV cell types. Natural melting of the snow layer requires almost 98% of generated power in cold regions (Alaska). The maximum energy savings brought forth by the pulse desnowing method is demonstrated in February for Chicago (0.41 kW h m⁻² for the GaAs PV cell) and in January for Alaska (8.3 kW h m⁻² for the GaAs PV cell) (Figure 5c). Our calculations present strong evidence to support the benefits of pulse desnowing.

Durability of the superhydrophobic surfaces proposed here is of great importance for ensuring long-term operation of the pulse desnowing technology. To evaluate the durability of our developed coating, we conducted multiple independent

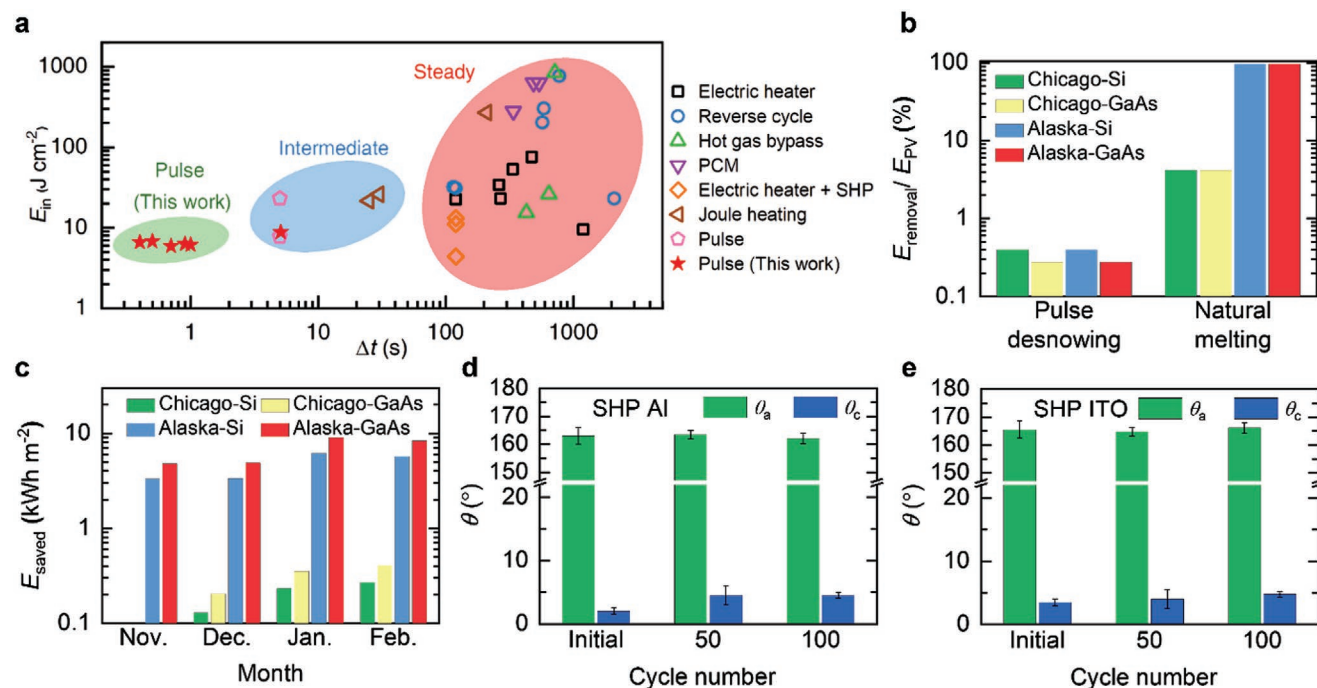


Figure 5. Energy savings, durability, and applicability. a) Benchmarking of the pulse method with state-of-the-art techniques by comparing the defrosting energy density and defrosting time. Results are divided into three zones: pulse (this work), intermediate, and steady. All references and comparisons are included in Table S1 (Supporting Information). b) Ratio of energy input for snow removal to PV cell power generation for the pulse method and natural melting method for weather conditions encountered in January 2020. c) Conserved energy (E_{saved}) by a PV cell on different months (November, December, January, and February) of year 2020 if pulse interfacial desnowing were used instead of no desnowing method (natural melting). Apparent advancing contact angle (θ_a) and contact angle hysteresis (θ_c) of d) SHP Al and e) SHP ITO surfaces showing the impact of extremely low temperature (-60°C) frosting/defrosting cycles.

durability tests. These include frosting/defrosting cyclic testing (Figure 5d,e; Note S5, Supporting Information), thermal testing (Note S6 and Video S7, Supporting Information), chemical exposure testing (corrosion and bare finger contact) (Notes S7 and S8, Figure S14, and Table S4, Supporting Information), mechanical scratch testing (Note S8 and Video S8, Supporting Information), low temperature exposure testing (Note S9, Videos S9 and S10, Supporting Information) and UV exposure testing (Note S10 and Figure S17, Supporting Information). The durability tests revealed that our boehmite-based coating is indeed reliable for the conditions tested, showing promising lab-scale potential for applicability with field testing still required. Figure 5d,e shows the effect of low temperature ($-60\text{ }^{\circ}\text{C}$) frosting/defrosting cycles on surface wettability for the SHP Al and the SHP ITO surfaces. The results reveal that the surfaces successfully survived 100 cycles of low temperature ($-60\text{ }^{\circ}\text{C}$) cycling, which is promising from an applicability standpoint. Experiments conducted to demonstrate pulsed Joule heating cycling durability showed no discernible change in pulse operation or accretion removal mechanisms after 20 cycles (see Video S7 and Figure S13, Supporting Information). Continued testing to 35 cycles showed no change in performance. Interestingly, pulsed interfacial defrosting was successful even on the damaged surfaces (see Video S8, Supporting Information) that is encouraging for real-world applications where handling during installation is inevitable and abrasion from dust and other moving objects may occur in operation. As a final robustness check, we successfully conducted pulse experiments at extremely low temperatures (-40 and $-100\text{ }^{\circ}\text{C}$) to demonstrate performance in harsh conditions (Note S9 and Videos S9 and S10, Supporting Information). Ice interlocking within nanostructures is a concern for elevated humidities.^[50] The robustness of the boehmite surface to interlocking depends on the morphology of the nanostructures.^[51] Icing and deicing robustness at high humidity ($\approx 70\%$) on nanostructured aluminum surfaces having similar structure morphologies and length scales demonstrated excellent resistance to interlocking at high humidities.^[52]

3. Discussion

The ability to achieve ultra-efficient snow, frost, and ice removal by pulsed Joule heating provides a potential pathway for enhancing the efficiency of both PV and wind installations in colder climates. Although not explicitly demonstrated here for wind turbines, integration with wind installations may be simpler due to the alleviated need for transparency. In addition to wind and PV, our ultra-rapid and ultra-efficient desnowing, defrosting, and deicing method helps to enable mass electrification of transportation (land, sea, and air) and building energy technologies (heating, ventilation, and air conditioning), where snow/frost/ice accretion present significant integration barriers and energy draws during mitigation.^[19] Furthermore, concentrated solar power (CSP) mirrors suffer from snowing, icing, water condensation, and soiling. Our multi-functional coating could provide a promising approach for CSP systems to enhance efficiency.^[53]

Unlike conventional resistive heaters, we take advantage of the integration of a thin-film heater with a superhydrophobic surface at the interface of the substrate and snow/frost/ice to achieve interfacial defrosting by confining the heat to a very thin region. The use of Joule heating for removal of snow (desnowing), frost (defrosting), and ice (deicing)²¹ is energetically demanding due to the large latent heat of solid to liquid phase change. Pulsed Joule heating drastically reduces the required energy and time for desnowing, defrosting, and deicing.^[22,23]

Durability of the coating is another important factor for the long-term stability of the pulse technology. Our study quantifies durability by conducting low temperature frosting/defrosting cycles (Note S5 and Figures S13 and S18, Supporting Information), pulse defrosting cycles (Note S6 and Video S7, Supporting Information), chemical stability analyses (Note S7, Figures S14 and S15, Table S4, Supporting Information), extremely low temperature exposure ($\approx -100\text{ }^{\circ}\text{C}$, Note S9, Videos S9 and S10, Supporting Information), UV exposure (Note S10 and Figure S17, Supporting Information), and scratching and abrasion tests (Note S8, Figure S16, and Video S8, Supporting Information). Although our pulse coating was able to successfully survive these durability tests, a need exists for additional studies focusing on durability mechanisms, quantification, and evaluation.^[54] Recently developed durable superhydrophobic coating designs having >1 year prolonged durability in wet conditions can be adopted to our technology to enhance robustness.^[55]

Large scale ($>1\text{ m}^2$) sputtering of thin films on various substrates (metals, glass, and polymers) and various substrate geometries (flat, convex, and concave) is established and used in multiple industries.^[56] The total cost of the large-scale deposition systems needs to be considered while conducting techno-economic analysis of our technology. As a potentially more cost-effective manufacturing alternative, aluminum-doped zinc oxide can be deposited using the sol-gel method.^[57] Furthermore, ITO deposition can be achieved using solution-based methods such as dip coating.^[58] The dip-coated materials need to be customized to achieve the resistivity and optical transparency that is acceptable for the application at hand. With mass production, fabrication costs will decrease and will potentially gain a foothold for application in PV and other renewable energy industries. Nonetheless, techno-socio-economic analysis of our technology represents an excellent opportunity for future study.

4. Conclusions

In summary, we have developed a coating to achieve ultra-rapid and ultra-efficient snow/frost/ice removal. We demonstrated pulsed electro-thermal interfacial desnowing through a combination of an ITO heating layer and boehmite nanostructures on a variety of substrates. Our method enables a three order of magnitude faster accretion removal time when compared to SOA approaches. Through experimental demonstrations, we found that the pulsed Joule heating for desnowing/defrosting process is divided into three different regimes of interfacial desnowing/defrosting, partial melting, and refreezing, depending on the energy input, pulse width, and inclination angle of the surface. To optimize the coating and method, we conducted numerical simulations to map the energy input as a

function of inclination angle, and melt layer fraction. We optimized the boehmite nanostructure and combination of coating strategy to achieve noninvasive snow removal by pulsed Joule heating. The outcomes of our work provide a scalable coating method to achieve accretion removal that is capable of being implemented in a variety of modern renewable energy systems based on PV and wind applications. This integration will help widen the penetration of these energy technologies to harsher climate regions.

Supporting Information

Supporting Information is available from the Wiley Online Library or from the author.

Acknowledgements

The authors gratefully acknowledge funding support from the National Science Foundation under Award No. 1554249 and the Air Conditioning and Refrigeration Center. N.M. gratefully acknowledges funding support from the International Institute for Carbon Neutral Energy Research (WPI-I2CNER), sponsored by the Japanese Ministry of Education, Culture, Sports, Science, and Technology. SEM, AFM, XPS, and sputtering were carried out in part in the Materials Research Laboratory Central Facilities, University of Illinois at Urbana-Champaign.

Conflict of Interest

The authors declare no conflict of interest.

Author Contributions

L.L. and S.K. contributed equally to this work. N.M., L.L., and S.K. conceived the idea. L.L., S.K., and K.F.R. fabricated all samples. L.L., S.K., and A.G. developed the pulse interfacial defrosting test setup. L.L. and S.K. performed pulse interfacial defrosting experiments, coating characterization, and PV performance tests. L.L., X.Y., and A.G. performed self-cleaning tests. S.K. performed the numerical simulations. L.L., S.K., and N.M. wrote the manuscript. N.M. supervised the project.

Data Availability Statement

The data that support the findings of this study are available in the supplementary material of this article.

Keywords

defrosting, deicing, desnowing, photovoltaic, pulsed Joule heating, self-cleaning, superhydrophobic, transparent

Received: February 7, 2022

Revised: March 16, 2022

Published online: May 2, 2022

[1] V. Scott, R. S. Haszeldine, S. F. Tett, A. Oschlies, *Nat. Clim. Change* **2015**, *5*, 419.

[2] a) M. Höök, X. Tang, *Energy Policy* **2013**, *52*, 797; b) J. Hansen, P. Kharecha, M. Sato, V. Masson-Delmotte, F. Ackerman,

- D. J. Beerling, P. J. Hearty, O. Hoegh-Guldberg, S.-L. Hsu, C. Parmesan, *PLoS One* **2013**, *8*, e81648.
- [3] a) G. Palmer, *Nat. Energy* **2019**, *4*, 538; b) F. Creutzig, P. Agoston, J. C. Goldschmidt, G. Luderer, G. Nemet, R. C. Pietzcker, *Nat. Energy* **2017**, *2*, 17140; c) B. Parida, S. Iniyar, R. Goic, *Renew. Sustain. Energy Rev.* **2011**, *15*, 1625; d) T. M. Razykov, C. S. Ferekides, D. Morel, E. Stefanakos, H. S. Ullal, H. M. Upadhyaya, *Sol. Energy* **2011**, *85*, 1580.
- [4] C. Breyer, D. Bogdanov, A. Gulagi, A. Aghahosseini, L. S. Barbosa, O. Koskinen, M. Barasa, U. Caldera, S. Afanasyeva, M. Child, *Prog. Photovoltaics* **2017**, *25*, 727.
- [5] B. Marion, R. Schaefer, H. Caine, G. Sanchez, *Sol. Energy* **2013**, *97*, 112.
- [6] N. Heidari, J. Gwamuri, T. Townsend, J. M. Pearce, *IEEE J. Photovolt.* **2015**, *5*, 1680.
- [7] R. E. Pawluk, Y. Chen, Y. She, *Renew. Sustain. Energy Rev.* **2019**, *107*, 171.
- [8] S. Kozarcin, H. Liu, G. B. Andresen, *Joule* **2019**, *3*, 992.
- [9] U.S. Energy Information Administration, https://www.eia.gov/state/seds/sep_prod/Prod_technotes.pdf, **2018**.
- [10] R. W. Andrews, A. Pollard, J. M. Pearce, *Sol. Energy* **2013**, *92*, 84.
- [11] M. M. D. Ross, report# EDRL 95-68 (TR), Energy Diversification Research Laboratory, CANMET. Natural Resources Canada, Varennes **1995**, p. 273.
- [12] R. W. Andrews, A. Pollard, J. M. Pearce, *Sol. Energy Mater. Sol. Cells* **2013**, *113*, 71.
- [13] A. Rahmatmand, S. J. Harrison, P. H. Oosthuizen, *Sol. Energy* **2018**, *171*, 811.
- [14] I. Czerniawska-Kusza, G. Kusza, M. Dużyński, *Environ. Toxicol.* **2004**, *19*, 296.
- [15] K. B. Karnauskas, J. K. Lundquist, L. Zhang, *Nat. Geosci.* **2018**, *11*, 38.
- [16] O. Fakorede, Z. Feger, H. Ibrahim, A. Ilinca, J. Perron, C. Masson, *Renew. Sustain. Energy Rev.* **2016**, *65*, 662.
- [17] N. Dalili, A. Edrisy, R. Cariveau, *Renew. Sustain. Energy Rev.* **2009**, *13*, 428.
- [18] a) ENERCON GmbH, *Enercon Magazine for Wind Energy* **2011**, *1*, 10; b) R. E. Bredesen, H. Refsum, presented at *IWAIS conference 2015*.
- [19] A. J. Mahvi, K. Boyina, A. Musser, S. Elbel, N. Miljkovic, *Int. J. Heat Mass Transfer* **2021**, *172*, 121162.
- [20] M. Elsharkawy, D. Tortorella, S. Kapatral, C. M. Megaridis, *Langmuir* **2016**, *32*, 4278.
- [21] a) V. F. Petrenko, C. R. Sullivan, V. Kozlyuk, F. V. Petrenko, V. Veerasamy, *Cold Reg. Sci. Technol.* **2011**, *65*, 70; b) S. Chavan, T. Foulkes, Y. Gurumukhi, K. Boyina, K. Rabbi, N. Miljkovic, *Appl. Phys. Lett.* **2019**, *115*, 071601; c) S. Khodakarami, L. Li, N. Miljkovic, *SPIE* **2021**, *11824*, 118240c.
- [22] T. L. Bergman, F. P. Incropera, D. P. DeWitt, A. S. Lavine, *Fundamentals of Heat and Mass Transfer*, John Wiley & Sons, New Jersey, USA **2011**.
- [23] D.-K. Yang, K.-S. Lee, *Int. J. Refrig.* **2004**, *27*, 89.
- [24] a) A. Nakajima, A. Fujishima, K. Hashimoto, T. Watanabe, *Adv. Mater.* **1999**, *11*, 1365; b) Q. Zhang, M. He, J. Chen, J. Wang, Y. Song, L. Jiang, *Chem. Commun.* **2013**, *49*, 4516.
- [25] D. Quéré, *Annu. Rev. Mater. Res.* **2008**, *38*, 71.
- [26] A. Lafuma, D. Quéré, *Nat. Mater.* **2003**, *2*, 457.
- [27] L. Li, Y. Lin, K. F. Rabbi, J. Ma, Z. Chen, A. Patel, W. Su, X. Ma, K. Boyina, S. Sett, *ACS Appl. Mater. Interfaces* **2021**, *13*, 43489.
- [28] T. Ishiguro, T. Hori, Z. Qiu, *J. Appl. Phys.* **2009**, *106*, 023524.
- [29] H. K. Raut, V. A. Ganesh, A. S. Nair, S. Ramakrishna, *Energy Environ. Sci.* **2011**, *4*, 3779.
- [30] H. K. Yu, W. J. Dong, G. H. Jung, J.-L. Lee, *ACS Nano* **2011**, *5*, 8026.
- [31] R. Gupta, K. D. Rao, S. Kiruthika, G. U. Kulkarni, *ACS Appl. Mater. Interfaces* **2016**, *8*, 12559.

- [32] Q. Huang, W. Shen, X. Fang, G. Chen, J. Guo, W. Xu, R. Tan, W. Song, *RSC Adv.* **2015**, *5*, 45836.
- [33] K. Rao, G. U. Kulkarni, *Nanoscale* **2014**, *6*, 5645.
- [34] a) P. Singh, S. K. Srivastava, B. Sivaiah, P. Prathap, C. M. S. Rauthan, *Sol. Energy* **2018**, *170*, 221; b) Y. Zhou, R. Azumi, S. Shimada, *Nanoscale* **2019**, *11*, 3804.
- [35] J. Hone, M. Llaguno, N. Nemes, A. Johnson, J. Fischer, D. Walters, M. Casavant, J. Schmidt, R. Smalley, *Appl. Phys. Lett.* **2000**, *77*, 666.
- [36] N. Gupta, S. Sasikala, D. B. Mahadik, A. V. Rao, H. C. Barshilia, *Appl. Surf. Sci.* **2012**, *258*, 9723.
- [37] N. Shanmugam, R. Pugazhendhi, R. Madurai Elavarasan, P. Kasiviswanathan, N. Das, *Energies* **2020**, *13*, 2631.
- [38] F. Chu, S. Gao, X. Zhang, X. Wu, D. Wen, *Appl. Phys. Lett.* **2019**, *115*, 073703.
- [39] R. Blossey, *Nat. Mater.* **2003**, *2*, 301.
- [40] M. J. Kreder, J. Alvarenga, P. Kim, J. Aizenberg, *Nat. Rev. Mater.* **2016**, *1*, 15003.
- [41] a) G. McHale, N. J. Shirtcliffe, M. I. Newton, *Langmuir* **2004**, *20*, 10146; b) S. Khodakarami, H. Zhao, K. F. Rabbi, N. Miljkovic, *ACS Appl. Mater. Interfaces* **2021**, *13*, 4519.
- [42] H. Teisala, M. Tuominen, M. Aromaa, M. Stepien, J. M. Mäkelä, J. J. Saarinen, M. Toivakka, J. Kuusipalo, *Langmuir* **2012**, *28*, 3138.
- [43] Y. Lai, X. Gao, H. Zhuang, J. Huang, C. Lin, L. Jiang, *Adv. Mater.* **2009**, *21*, 3799.
- [44] a) I. Nayshevsky, Q. F. Xu, G. Barahman, A. M. Lyons, *Sol. Energy Mater. Sol. Cells* **2020**, *206*, 110281; b) S. L. Moffitt, R. A. Fleming, C. S. Thompson, M. F. Toney, L. T. Schelhas, presented at *IEEE 7th World Conference on Photovoltaic Energy Conversion (WCPEC)*, June **2018**; c) S. L. Moffitt, R. A. Fleming, C. S. Thompson, C. J. Titus, E. Kim, L. Leu, M. F. Toney, L. T. Schelhas, *ACS Appl. Energy Mater.* **2019**, *2*, 7870.
- [45] a) K. M. Wisdom, J. A. Watson, X. Qu, F. Liu, G. S. Watson, C.-H. Chen, *Proc. Natl. Acad. Sci. USA* **2013**, *110*, 7992; b) K. Zhang, F. Liu, A. J. Williams, X. Qu, J. J. Feng, C.-H. Chen, *Phys. Rev. Lett.* **2015**, *115*, 074502.
- [46] M. D. Mulroe, B. R. Srijanto, S. F. Ahmadi, C. P. Collier, J. B. Boreyko, *ACS Nano* **2017**, *11*, 8499.
- [47] X. Yan, L. C. Zhang, S. Sett, L. Z. Feng, C. Y. Zhao, Z. Y. Huang, H. Vahabi, A. K. Kota, F. Chen, N. Miljkovic, *ACS Nano* **2019**, *13*, 1309.
- [48] X. Yan, Z. Huang, S. Sett, J. Oh, H. Cha, J. Li, L. Feng, W. Yifan, Z. Chongyan, D. Orejon, F. Chen, N. Miljkovic, *ACS Nano* **2019**, *13*, 4160.
- [49] <https://www.weather.gov/wrh/Climate> (accessed: September 2021).
- [50] J. Chen, J. Liu, M. He, K. Li, D. Cui, Q. Zhang, X. Zeng, Y. Zhang, J. Wang, Y. Song, *Appl. Phys. Lett.* **2012**, *101*, 111603.
- [51] X. Wu, V. V. Silberschmidt, Z.-T. Hu, Z. Chen, *Surf. Coat. Technol.* **2019**, *358*, 207.
- [52] A. Kim, C. Lee, H. Kim, J. Kim, *ACS Appl. Mater. Interfaces* **2015**, *7*, 7206.
- [53] a) K. Ilse, L. Micheli, B. W. Figgis, K. Lange, D. Daßler, H. Hanif, F. Wolfertstetter, V. Naumann, C. Hagendorf, R. Gottschalg, *Joule* **2019**, *3*, 2303; b) A. Sayyah, M. N. Horenstein, M. K. Mazumder, presented at *2013 IEEE 39th Photovoltaic Specialists Conference (PVSC)*, Tampa Bay, Florida, June **2013**.
- [54] J. Ma, S. Sett, H. Cha, X. Yan, N. Miljkovic, *Appl. Phys. Lett.* **2020**, *116*, 260501.
- [55] J. Ma, Z. Zheng, M. J. Hoque, L. Li, K. F. Rabbi, J. Y. Ho, P. V. Braun, P. Wang, N. Miljkovic, *ACS Nano* **2022**, *16*, 4251.
- [56] a) AGC Plasma Technology Solutions, Magnetron Sputtering Equipment, <https://www.agc-plasma.com/technologies/#magnetron-sputtering-equipment> (accessed: December 2021); b) R. Kukla, *Surf. Coat. Technol.* **1997**, *93*, 1.
- [57] A. R. Phani, M. Passacantando, S. Santucci, *Mater. Chem. Phys.* **2001**, *68*, 66.
- [58] H.-D. Kim, M. J. Yun, J. H. Lee, K. H. Kim, T. G. Kim, *Sci. Rep.* **2014**, *4*, 4614.